Nanoelectronics and Its New Materials – A NEW ERA OF NANOSCIENCE

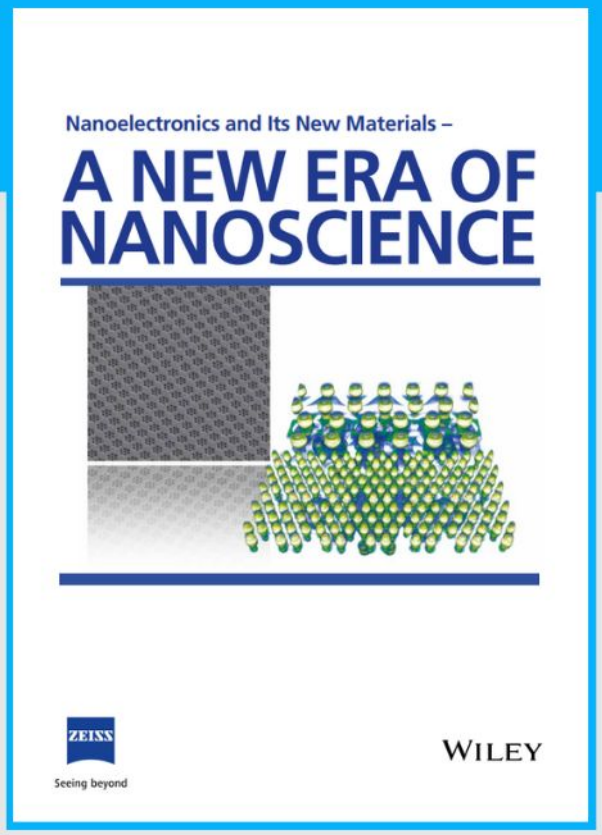

Discover the recent advances in electronics research and fundamental nanoscience.

Nanotechnology has become the driving force behind breakthroughs in engineering, materials science, physics, chemistry, and biological sciences. In this compendium, we delve into a wide range of novel applications that highlight recent advances in electronics research and fundamental nanoscience. From surface analysis and defect detection to tailored optical functionality and transparent nanowire electrodes, this eBook covers key topics that will revolutionize the future of electronics.

To get your hands on this valuable resource and unleash the power of nanotechnology, simply download the eBook now. Stay ahead of the curve and embrace the future of electronics with nanoscience as your guide.

ZEISS

Seeing beyond

WILEY

NANO · MICRO small
www.small-journal.com

In Situ Atomic-Scale Observation of Electrochemical (De)potassiation in Te Nanowires

*Fang Liu, Jiashen Meng, Hong Wang, Shulin Chen, Ruohan Yu, Peng Gao, and Jinsong Wu**

Potassium-ion batteries (PIBs) have great potential in energy storage due to their high abundance and low cost of potassium resources. Tellurium (Te) is a promising PIB cathode due to its high volumetric capacity and good electronic conductivity. However, the electrochemical (de)potassiation mechanism of Te remains elusive due to the lack of an effective method of directly observing the dynamic reaction at atomic resolution. Here, the phase transformations of single crystal Te on (de)potassiation are clearly revealed by in situ high-resolution transmission electron microscopy and electron diffraction. Te undergoes a consecutive phase transformation during potassiation: from Te to K_2Te_3 in the initial potassiation, and then part of the K_2Te_3 to K_5Te_3 on further potassiation. The reaction has extremely high reversibility in the following depotassiation. By atomic-scale observation, an anisotropic reaction mechanism where K^+ intercalates into Te crystalline lattice preferentially through the (001) plane (having a large *d*-spacing) is established during potassiation. While in the depotassiation process, K ions extract from the polycrystalline K_xTe along the same diffusion path to form single crystal Te, indicating the potassium storage is highly reversible. The strong orientation-dependent (de)potassiation mechanism revealed by this work provides implications for the future design of nanostructured cathodes for high-performance PIBs.

1. Introduction

Potassium-ion batteries (PIBs) have recently aroused worldwide attention for energy storage in the applications of electric vehicles and smart grids due to their low cost, abundant resource, and low redox potential of K^+/K (−2.93 V vs standard hydrogen potential).[1,2] However, finding suitable electrode materials for PIBs is still challenged by the large ionic radius of K^+, significantly impacting the ionic transport and storage capability within electrodes run on intercalation reactions.[3,4] Recently, high-capacity electrode materials for PIBs based on other types of reaction have been discovered such as the alloy/conversion-type materials (e.g., phosphorus, antimony, bismuth, and sulfur).[5–9] In particular, conversion-type sulfur (S)- and selenium (Se)-based PIBs are capable of delivering high theoretical gravimetric capacities.[9–12] However, their intrinsic low electronic conductivity and sluggish reaction kinetics lead to inferior electrochemical performance.[13–15] Among chalcogenide elements, tellurium (Te) exhibits high electronic conductivity (2×10^2 S m^{-1}), which leads the path to a promising application in PIB with a remarkable rate of performance at a high current density.[16–19]

While a large amount of research activity has focused on lithium and sodium-ion batteries, there are not too many literatures in the field of PIBs.[20–22] Although Te is tested as a cathode for PIBs, the proposed reaction mechanisms remain controversial. Shuai et al. reported a Te/porous carbon composite for KIB, delivering a high capacity and rate performance. The electrode material undergoes a two-electron conversion reaction forming the K_2Te phase in potassiation, as revealed by ex situ transmission electron microscopy (TEM), X-ray powder diffraction (XRD), X-ray photoelectron spectroscopy analyses (XPS), and theoretical calculations.[16] Meanwhile, Qin et al. reported that Te undergoes stepwise conversion reactions and transforms first to soluble K_2Te_3 polytelluride and ultimately to insoluble K_5Te_3 compound in potassiation, as revealed by UV–vis absorption spectroscopy, XRD, and XPS.[17]

Meanwhile, atomic-scale observation is needed to reveal the details of the reaction mechanisms such as how K ions react with the host atoms and how the reaction interface evolves.[23–25] Also, it is urgent that the dynamic reaction processes can be unveiled by the advanced real-time in situ methods in order to further improve the performance of K–Te batteries.[25,26]

F. Liu, J. Meng, H. Wang, R. Yu, J. Wu
State Key Laboratory of Advanced Technology for Materials Synthesis and Processing
School of Materials Science and Engineering
Wuhan University of Technology
Wuhan 430070, P. R. China
E-mail: wujs@whut.edu.cn

F. Liu, H. Wang, R. Yu, J. Wu
Nanostructure Research Center (NRC)
Wuhan University of Technology
Wuhan 430070, P. R. China

S. Chen, P. Gao
Electron Microscopy Laboratory
School of Physics
Peking University
Beijing 100871, P. R. China

The ORCID identification number(s) for the author(s) of this article can be found under https://doi.org/10.1002/smll.202200844.

DOI: 10.1002/smll.202200844

In situ TEM technique has been developed as a powerful tool to track electrochemical reactions of electrode materials on the nanometer scale in real time.[27–29] It has the unique merit of providing direct insights into dynamic compositional and microstructural evolutions during electrochemical reactions in electrodes.[21,30]

Here, we explore the atomistic (de)potassiation mechanism of single crystalline Te nanowires (NWs) using both in situ X-ray diffraction and in situ TEM including high-resolution transmission electron microscopy (HRTEM) imaging and dynamic electron diffraction (ED).[31] We discover a two-step potassiation mechanism involving a Te-to-K_2Te_3 transition in the first stage and an incompletely K_2Te_3-to-K_5Te_3 transition in the second stage. The final potassiation products are the mixture of K_2Te_3 and K_5Te_3. During depotassiation, Te forms due to the extraction of K ions from K_2Te_3 and K_5Te_3, which is a highly reversible deconversion process. It is further discovered that the diffusion of K ions within the Te NW is through a definite pathway, that is, along the close-packed (001) plane by the anisotropic reaction. Furthermore, we observe for the first time the depotassiation process at the atomic scale and find the extraction of K ions occurs reversibly along the (001) plane as well, leading to the formation of a Te single crystal with the same crystal orientation as the original Te NWs. The full reversibility of crystal orientation on (de)potassiation helps us to design cathodes for high-rate performance PIBs in the future.

2. Results and Discussion

2.1. Structure Analysis of Te NWs

The phase of the as-synthesized Te NWs was identified by XRD. As shown in **Figure 1**a, the pattern can be well indexed to the pure Te hexagonal phase (JCPDS card no. 01-086-2268, with lattice parameters of a = 7.62 Å, b = 4.31 Å, c = 6.00 Å, $\alpha = 90°$, $\beta = 90.788°$, and $\gamma = 90°$) without any impurity.[32] Low-magnification TEM image indicates that the sample has nanowire morphology with a diameter of ≈10–100 nm (Figure 1b). The 1D Te NW is identified to grow along the [010] direction in Figure 1d. The atomic model of a single Te crystal along the [010] direction is shown in Figure 1c. Its HRTEM image and Fast Fourier Transformation (FFT) pattern show ordered lattice fringes with spacing distances of 3.8 and 6.0 Å, corresponding to the (200) and (001) planes of Te, respectively (Figure 1e,f). Its composition is further confirmed by X-ray energy dispersive spectroscopy (EDS) (Figure 1g). Another Te NW along the [110] zone axis is imaged by the high-angle annular dark-field scanning tranmission electron microscopy (HAADF-STEM) image as shown in Figure S1a, Supporting Information, in which the lattice planes with d-spacing of 2.3 and 3.2 Å are indexed to be the (1-12) and (1-1-1) planes, respectively. The enlarged STEM image (Figure S1b, Supporting Information) matches well with the atomic model of a single Te crystal projected along the [110] direction (Figure S1c, Supporting Information).

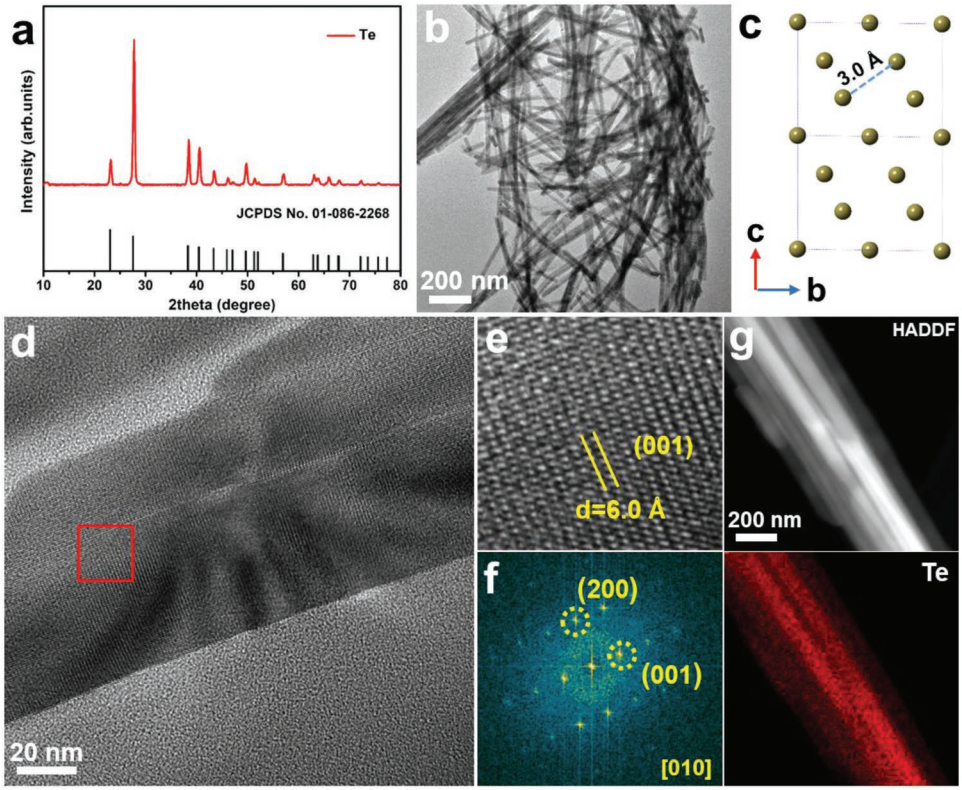

Figure 1. Structure and morphology characterization of Te NWs. a) XRD pattern, b) TEM images, c) crystal structure model of the hexagonal Te closed to the [010] zone axis, d) TEM image, e) A HRTEM image of the Te NW (d), f) the corresponding FFT image. g) A HAADF-STEM image and the corresponding STEM-EDS mapping of Te.

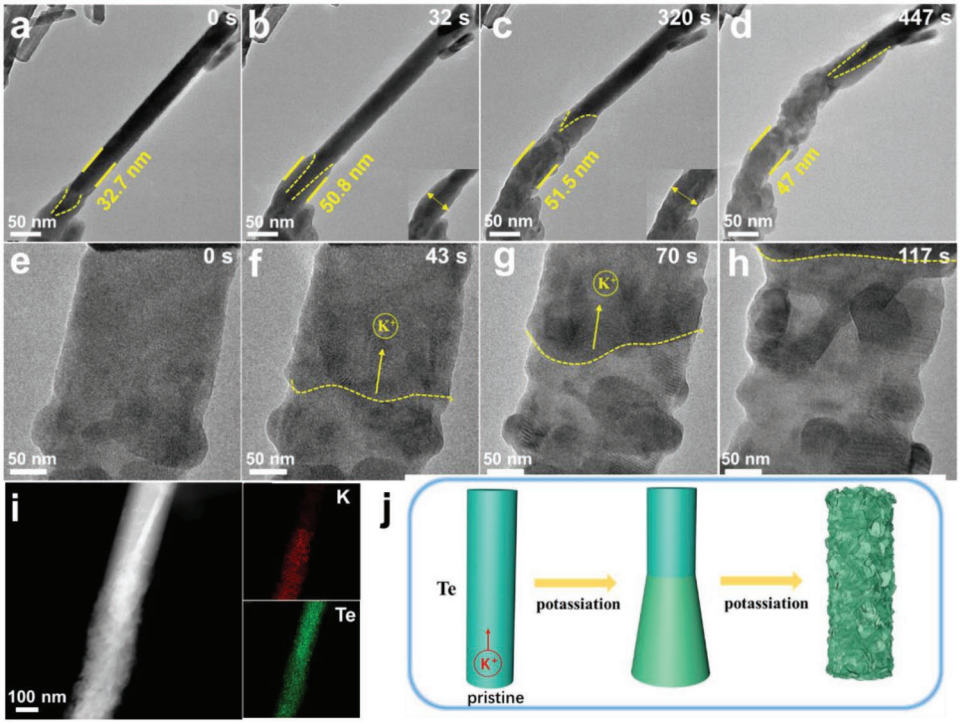

Figure 2. a–d) Chronological TEM images show the morphological evolution of the Te NW during the first potassiation process. Obvious volume expansion is visible. e–h) Chronological TEM images show the morphological evolution of the other Te NW during the first potassiation process. i) A HAADF-STEM image and the corresponding STEM-EDS mapping of the potassiated Te NW. j) A schematic illustration of morphological evolution during the first potassiation of the Te NWs.

2.2. The Morphological Evolution during Potassiation Process

To investigate electrochemical (de)potassiation behaviors of Te NWs, miniature and all-solid PIBs consisting of individual Te NWs as cathodes are constructed inside a TEM for in situ electrochemical experiments, as schematically shown in Figure S2, Supporting Information.[33,34] The morphological evolutions of Te NWs upon potassiation are also shown in Movies S1 and S2, Supporting Information. Upon applying a potential of –1 V, the K ions diffuse forward from the point of contact between the Te NW and the K resource. **Figure 2**a–d shows the chronological TEM images of Te NW during the potassiation process. The surficial area of the Te NW expands much quicker than the core, indicating a radially surface-to-core diffusion mechanism (Figure 2a–d). By measuring the diameter of the nanowire in potassiation from 0 to 32 s, the original diameter of ≈32.7 nm is gradually expanded to ≈50.8 nm (with a corresponding volume expansion of ≈55.3%). At 320 s, potassiated-Te polycrystals with a grain size up to 20 nm can be clearly seen, demonstrating nucleation and growth of new crystals during potassiation (Figure 2c). The diameter increases from 50.8 to 51.5 nm at this stage. When it is 447 s, the elongation of the potassiated nanowire leads to the diameter shrinkage from 51.5 to 47 nm and bending as well (Figure 2d). Figure 2e–h and Figure S3, Supporting Information, show a series of TEM images of the other Te NWs with similar morphological evolutions during the potassiation process. The reaction fronts (RFs) marked with yellow dashed lines gradually propagated along the radial direction. Grains with a size of ≈20 nm are gradually formed inside the nanowire with the progress of potassiation. A chronologically enlarged view in region 1 of the potassiated Te NW (Figure S4, Supporting Information) demonstrates one grain gradually grows large as outlined by the yellow dash line. The crystal can be identified as the K_2Te_3 phase with the (020) plane indexed by the corresponding FFT pattern (Figure S4, Supporting Information). Figure S5, Supporting Information, shows chronologically HRTEM images of the enlarged region 2 (marked in Figure S3, Supporting Information). The crystal outlined by the yellow line is also identified as the K_2Te_3 phase, which gradually grows into a large crystal showing clearly the (012) plane upon potassiation.

The compositional change is also monitored by the HAADF-STEM image and the EDS mapping. As shown in Figure 2i, in the partially potassiated Te NW, Te and K elements are evenly distributed in the potassiated region, showing K diffusion in Te NW during the potassiation process. The schematic illustration in Figure 2j vividly highlights the aforementioned morphological evolutions during the potassiation process of a Te NW.

2.3. The Phase Evolution during Potassiation and Depotassiation

Dynamic ED patterns were recorded to identify the sequential crystalline phase transformation of Te NW during potassiation

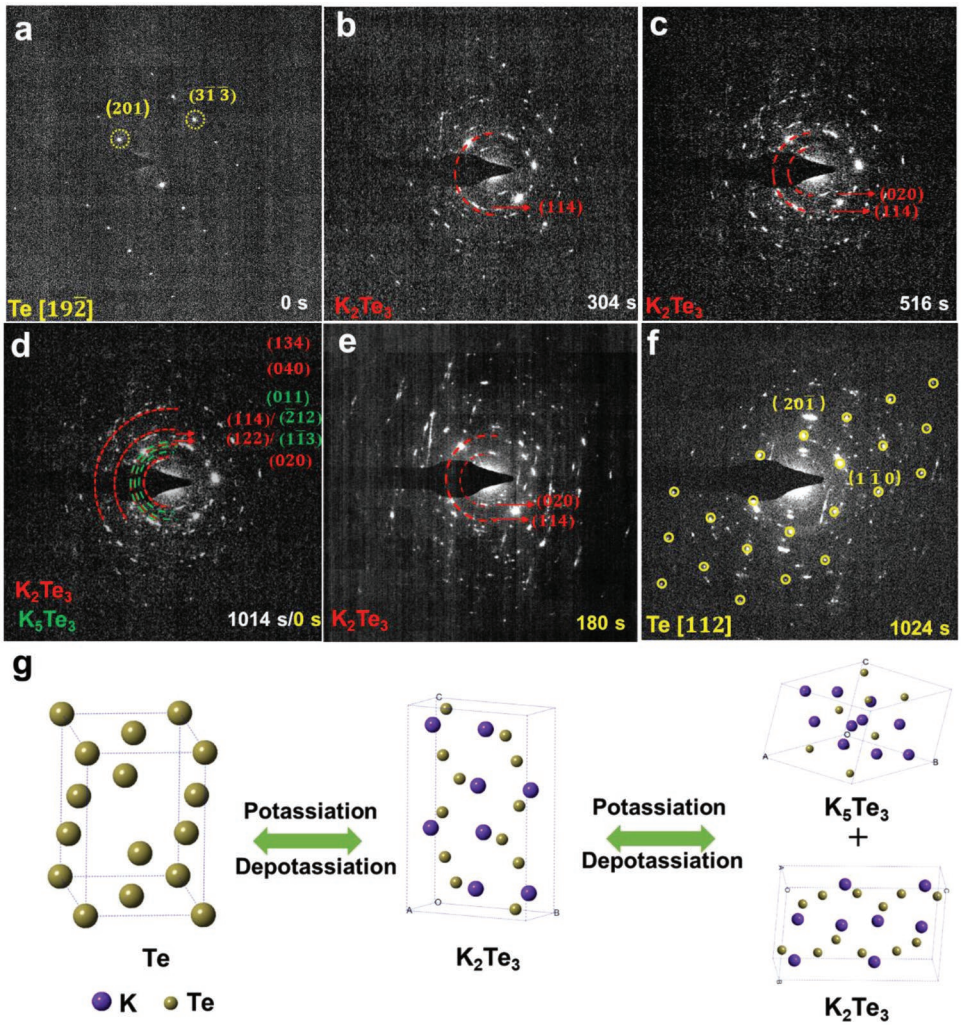

Figure 3. a–c) Consecutive SAED patterns to identify phase evolutions of the Te NW during the potassiation process. d–f) Consecutive SAED patterns to identify phase evolutions of the potassiated Te NW during the depotassiation process. g) An atomic illustration of the phases formed during the first potassiation and depotassiation.

and depotassiation, as shown in **Figure 3** (see also Movie S3, Supporting Information). Before potassiation, a pristine Te NW with a diameter of 73.4 nm shows its single crystalline nature, where the diffraction spots marked by a yellow dotted ring can be indexed as close to the [19-2] zone axis of the Te phase (Figure 3a and Figure S6a, Supporting Information). Upon potassiation, some diffraction spots of pristine structure gradually disappear and the diffraction rings, indexed as the (114) and (020) plane of K_2Te_3, become brighter, confirming the conversion reaction in the first stage (Figure 3b,c). After further potassiation to 1014 s, all diffraction spots of Te crystal disappear and new diffraction rings appear in the second stage, which can be indexed as the {122}, {040}, and {134} reflections of K_2Te_3 and the {-212}, {1-13}, and {011} reflections of K_5Te_3. The partial transformation from K_2Te_3 into the K_5Te_3 phase may be attributed to slow reaction kinetics between K_2Te_3 and K. Meanwhile, the diameter after potassiation expands from ≈73.4 to ≈83.4 nm (Figure S6b, Supporting Information).

The phase evolution of the potassiated Te during the depotassiation process was further analyzed by the selected area electron diffraction (SAED) patterns in Figure 3d–f. Upon depotassiation to 180 s, the diffraction rings of the {-212}, {1-13}, and {011} reflections of K_5Te_3 disappear and only the {122} and {040} reflections of K_2Te_3 phase can be detected, indicating that the deconversion reaction of K_5Te_3 occurs in the initial stage of depotassiation (Figure 3e). After 1024 s of depotassiation, almost all of the diffraction rings of the K_2Te_3 phase disappear as shown in Figure 3f. Significantly, the diffraction pattern shows the formation of single crystal Te along the [112] zone axis (Figure 3f). The recovery of single crystalline Te in the depotassiation shows robust reversibility of thin Te NWs during K electrochemical reactions. After full depotassiation, the extraction of K^+ led to an obvious radial contraction of the Te NW from ≈83.4 to ≈73.2 nm (Figure S6c, Supporting Information). Such a reversible phase transition in potassiation and depotassiation is illustrated by the atomic models as shown in Figure 3g. Here, the final potassiated product is identified as a mixture of K_2Te_3 and K_5Te_3 phase, which could be resulted from an incomplete conversion reaction.

2.4. The Anisotropic and Reversible Potassiation and Depotassiation Observed by Atomic-Scale Imaging

To further understand the underlying potassiation mechanisms of Te NWs, in situ HRTEM imaging was performed to track localized phase structure in real time (Movie S4, Supporting Information).[35] Figure S7, Supporting Information, shows chronological TEM images of two adjacent Te NWs on potassiation, in which only NW 1 directly contacts the potassium source. Two original Te NWs have the same crystal orientation which is along the [010] zone axis, and the same growth direction (along the [001] direction). Upon potassiation, reaction fronts marked with yellow dashed lines began to appear on NW 1 and gradually propagated along the (001) lattice plane to NW 2. It implies that K ions diffuse faster along the (001) plane, which has a large *d*-spacing and a large Te-Te channel enabling ion diffusion. After potassiation for some time, Moire fringe can be observed (Figure S7c, Supporting Information) and the contrast of the fringe becomes enhanced with increased potassiation time as shown in Figure S7d, Supporting Information. This implies that on the top of the Te crystal, the other type of crystal (i.e., K_2Te_3) forms. It indicates that K ions intercalate preferentially into crystalline Te along the (010) plane as well (next to the (001) plane, which is the fastest diffusion path), leading to a slice-by-slice potassiation. When the K atom diffused on the surface of another neighboring Te NW 2, we can see two types of RFs, marked by a blue dotted line (interface 1) and an orange dotted line (interface 2) in Figure S7e–l, Supporting Information. The migration rate of interface 1, mainly parallel to the [001] direction, was faster than interface 2. It was attributed to the fastest diffusion path of K ion along the (001) plane.

Figure 4a1–d1 shows the chronological HRTEM image of the thin edge of the Te NW during potassiation. The corresponding enlarged HRTEM images and FFT patterns chosen from the marked regions in Figure 4a1–d1 are shown in Figure 4a2–d2,a3–d3. The unreacted Te is indexed along the [010] zone axis. After 305 s of potassiation, the K_2Te_3 phase forms at the edge, which is along the [1-10] zone axis as identified by the enlarged HRTEM images (Figure 4b2) and FFT pattern (Figure 4b3). Here, an orientation relationship between Te and K_2Te_3 can be determined: [010]_Te//[1-10]_K_2Te_3, (200)_Te//(110)_K_2Te_3 (with a misfit of 11%), and (001)_Te//(002)_K_2Te_3 (with misfit of 33%). Therefore, the K_2Te_3 crystal grows faster in the (002) lattice plane than in the other lattice plane. Similar to the ledge mechanism, a zigzag interface of Te and K_2Te_3 forms in the (200) plane (referring to Te crystal) as the (002) plane, which is the fastest diffusion path as outlined in Figure 4b1. As shown in Figure S6d, Supporting Information, multiple formed plate-like nanocrystals can be observed after the potassiation of 323 s. The size of these plate-like nanocrystals continuously increases with increased potassiation time as shown in Figure S6d–I, Supporting Information. After the potassiation of 826 s, part of the plate-like K_2Te_3 nanocrystals overlaps with unreacted Te (Figure 4c1). Meanwhile, the interface of Te and K_2Te_3 moves toward the (200) plane. The new K_2Te_3 crystal domain can be indexed along the [-321] zone axis as shown in Figure 4c2,3, showing inhomogeneous growth of K_2Te_3. When the potassiation reaction goes on to 1047s, the K_2Te_3 phase gradually transforms into the K_5Te_3 phase. K_5Te_3 phase is indexed

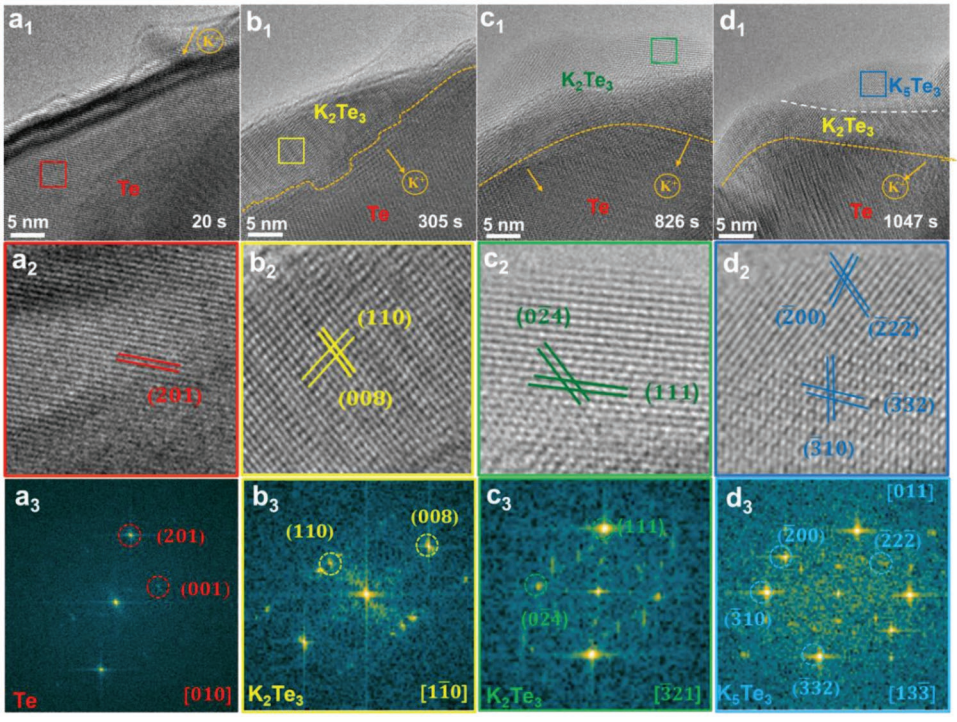

Figure 4. a_1–d_1) Time-sequenced HRTEM images of the potassiation process of Te, which is an enlarged view of the region marked by a red square in Figure S5a, Supporting Information. a_2–d_2) HRTEM images and a_3–d_3) corresponding FFT patterns taken from the regions marked by the squares in (a_1–d_1), respectively.

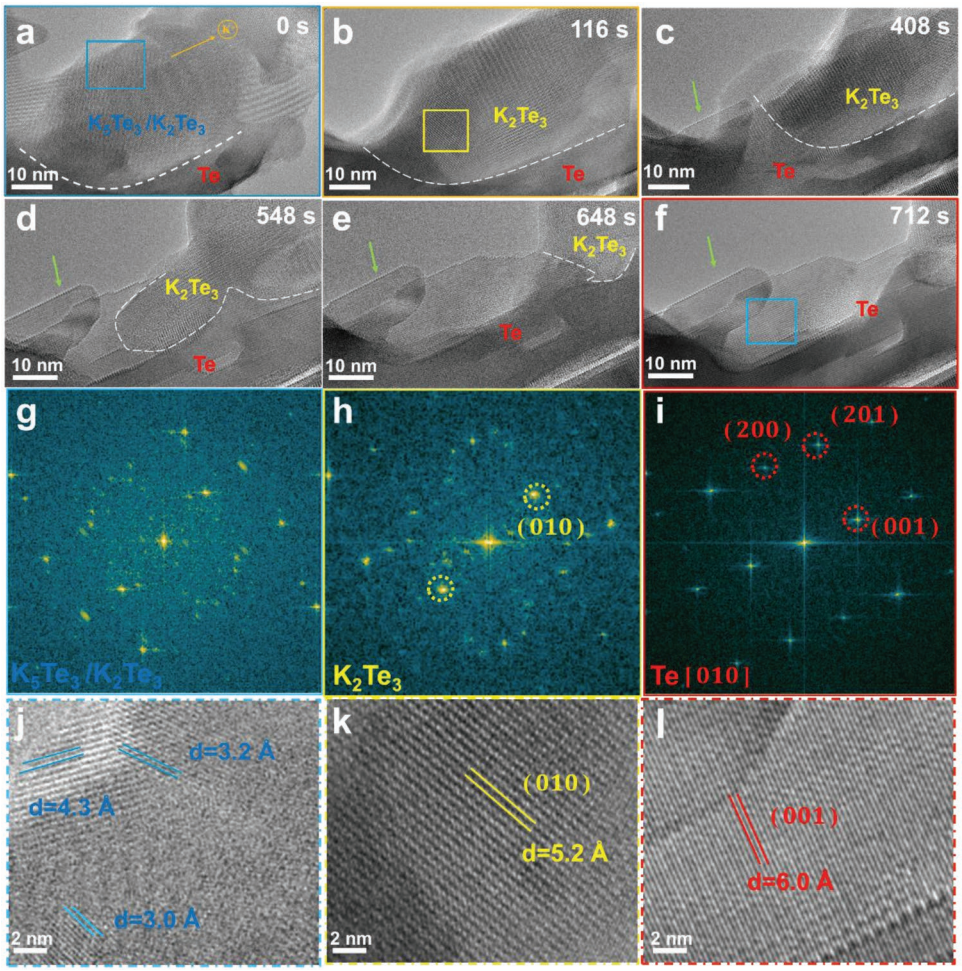

Figure 5. a–f) HRTEM images show the morphological evolution of the Te NW during the depotassiation process. g–i) The corresponding FFT patterns taken from the regions marked by the squares in (a), (b), and (f), respectively. j–l) Enlarged HRTEM images taken from the regions marked by the squares in (a), (b), and (f), respectively.

along the [13-3] zone axis as shown in Figure 4d_{1-3}. Phase evolution in other areas is also analyzed and a similar phase transition process is identified (Figure S8, Supporting Information).

The depotassiation process of the potassiated NWs is studied to reveal the phase transitions during extraction of the K ions (Movie S5, Supporting Information). A constant positive potential of 1 V was applied on the potassiated Te NW to initiate the desodiation process. **Figure 5**a and Figure S9a, Supporting Information, show HRTEM images of a partially potassiated Te NW. The interface (marked by white dashed lines) divides the NW into two distinct regions. The region on the top has a polycrystal K_xTe phase, proved by the FFT pattern and the enlarged HRTEM image (Figure 5g,j). While the region at the bottom is the unreacted Te single crystal along the [010] zone axis, and the interface is mainly parallel to the [001] direction (referring to the Te crystal). After 116 s of depotassiation, the K_xTe region shrinks progressively and the K_5Te_3 phase gradually disappears (Figure 5b), while K_2Te_3 remains as the major phase (Figure 5h,k). After 408 s of depotassiation, a Te single crystal marked by the green arrow appears (Figure 5c), demonstrating the reversibility of the deconversion reaction. After 548 s, the Te single crystal grows along the [001] direction and becomes large (Figure 5c–f and Figure S9, Supporting Information). At 712 s, the potassiated Te completely transforms into a Te single crystal (Figure 5f). The formed Te nanocrystal can be indexed along the [010] zone axis as shown in the HRTEM image and corresponding FFT patterns (Figure 5i,l). It has the same crystal orientation as the pristine Te NW. A similar transformation from polycrystalline K_xTe to single crystal Te upon depotassiation was observed in the other area (Figure S10, Supporting Information). The depotassiation process from K_5Te_3/K_2Te_3 phase to the K_2Te_3 phase and finally to single phase Te can be vividly shown in the schematic illustration (**Figure 6**a).

Due to the lattice plane of Te nanowire with different *d*-spacing, the diffusion rate of K^+ into Te nanowire along different lattice planes is different, resulting in the anisotropic reaction mechanism during potassiation. The anisotropic reaction gives rise to drastic phase changes and volume expansion in different orientations, which is unfavorable for the reversibility of the electrode reaction. However, when the growth direction of Te is along the [001] direction, K^+ can quickly diffuse into Te nanowire along the (001) plane by the anisotropic

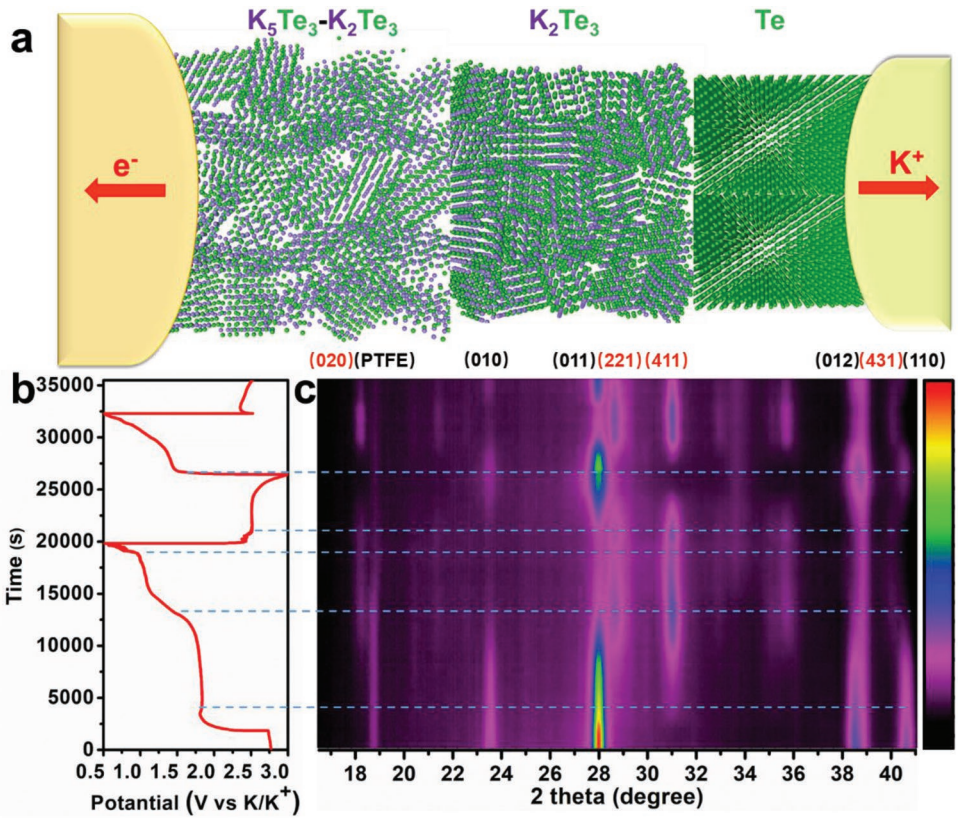

Figure 6. a) Schematic illustration of potassiation of Te NWs. Three different phases appeared in potassiation due to the alloying reaction. b) Discharge/charge curves during the first two cycles at 0.05 A g^{-1} in 0.5–3 V of Te NWs. c) 2D in situ XRD pattern collected in the range of 16°–41°.

reaction mechanism. Meanwhile, the potassiated Te can completely transform into single Te in such nanowire with the [001] direction as growth direction, implying that the reaction has extremely high reversibility. On depotassiation, K^+ can extract from K_5Te_3/K_2Te_3 to prompt the rearrangement of the Te atom in the (002) plane. The strong orientation-dependent (de)potassiation mechanism revealed by this work provides implications for the future design of nanostructured cathodes for high-performance PIBs.

2.5. The Phase Structure Evolution at Electrode Level Using In Situ XRD

The crystalline structure evolution of Te NWs was further monitored using in situ XRD measurements to confirm the K ion de-intercalation/intercalation mechanism (Figure 6b,c).[36,37] The voltage profile as a function of (dis)charge capacity during the second cycle is shown in Figure 6b. During potassiation, the profile shows two long plateaus with the first one at ≈1.7 V and the second one at ≈1 V in the first cycling, indicating that the potassiation of Te is characteristic of two-phase reactions. Figure 6c shows that the as-fabricated Te electrode exhibits the characteristic peaks of the (010), (011), (012), and (110) at 23.0°, 27.5°, 38.2°, and 40.4°, respectively. When the cell gradually discharged to 1.7 V, the intensity of each diffraction peak gradually decreased and new diffraction peaks corresponding to the (020), (221), (411), and (431) planes of the K_2Te_3 phase appeared at about 17.0°, 28°, 30.7°, and 39.4°, indicating that K^+ is gradually inserted into Te NWs with the formation of K_2Te_3 phase in the first stage of potassiation. When discharging to 1.5 V, Te diffraction peaks totally disappear and the intensity of K_2Te_3 peaks increases to the maximum, implying that Te has been completely transformed into K_2Te_3 by conversion reaction. The intensity of K_2Te_3 peaks gradually decreases and no new peak appears when discharging to 1 V, implying the formation of the other K_xTe phase in this process. However, K_2Te_3 peaks still exist even after discharging to 0.5 V, indicating that the final potassiation product is the K_2Te_3 phase and K_xTe phase. Combined with the SAED pattern, the K_xTe phase should be the K_5Te_3 phase, although it is not clearly identified by XRD due to the small portion in the mixed phases and slow kinetics of the transition from K_2Te_3 to K_5Te_3. Upon charging, the signals of K_2Te_3 can be observed and its intensity gradually increases to the maximum when charging to 2.5 V, implying the disappearance of the K_5Te_3 phase. With further charging, the intermediate phase of K_2Te_3 gradually transformed into the Te phase, proving its full reversibility of the deconversion reaction.

Figure S11, Supporting Information, presents the first three cyclic voltammetry (CV) curves of the Te cathode in the voltage window of 0.5–3 V at a scan rate of 0.1 mV s^{-1}. Two cathodic peaks at 1.75 and 1 V can be seen in the first cycles, indicating the two-phase reaction during potassiation. There are two anodic peaks at 2.05 and 2.42 V in the first cycles, corresponding to the reversible extraction of K ions. The observed multiple redox peaks are consistent with the result of in situ

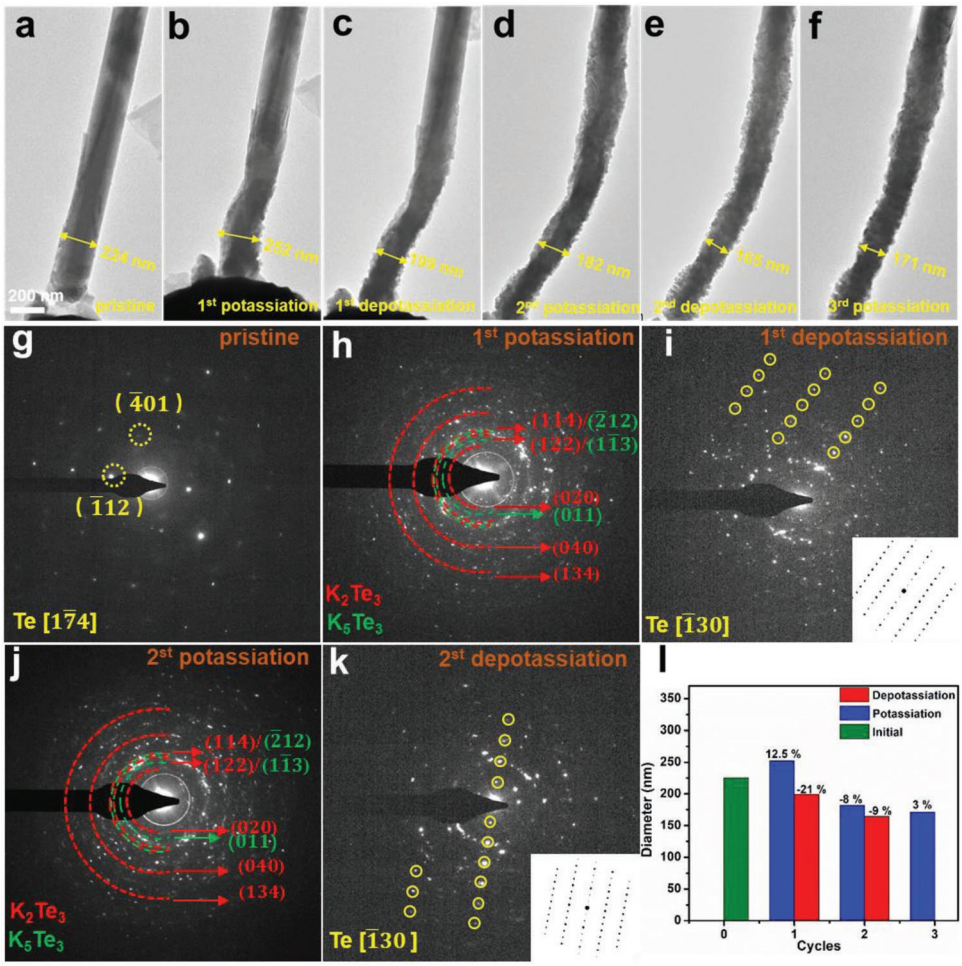

Figure 7. a–f) Microstructure evolutions of the Te NW during the first three potassiation/depotassiation processes. The NW exhibits repeated volume expansion and contraction in cycling. g–k) SAED patterns show phase evolutions during the first two cycles of potassiation/depotassiation of the Te NW. l) The measured diameters versus the cycling number of the Te NW.

TEM. The cycling performance of Te electrodes is presented in Figure S11b, Supporting Information. The specific capacity during the first cycles is 500 mAh g^{-1}, the capacity decay during the subsequent cycles can be seen due to the huge volume expansion of pure Te nanowires. Figure S12a, Supporting Information, show ex situ TEM images of the Te electrode at different states. When discharging to 0.5 V, the single Te nanowire transforms into K_5Te_3 nanoparticles as shown in Figure S12, Supporting Information. A K_5Te_3 crystal closed to the [-1-10] zone axis is identified by the HRTEM image and its corresponding FFT pattern (Figure S12b,c, Supporting Information). After charging to 3 V, the K_5Te_3 phase is reversibly transformed into Te crystal (Figure S12d–f, Supporting Information), which is consistent with the in situ TEM results.

2.6. The Morphology and Phase Evolution of Te during Multi-Cycle (De)potassiation

To figure out the overall potassiation storage mechanism, multi-cycle (de) potassiation processes of Te were subsequently investigated, as shown in **Figure 7**.[38] The Te NW in Figure 7a–f undergoing multicycle (de)potassiation can withstand repeated volume expansion and contraction, implying its feasibility for electrode material of rechargeable PIBs. Figure 7l displays the radial expansion and contraction rates for each electrochemical cycle. Figure 7g–k presents the SAED patterns of the Te NW in the first two cycles. The SAED pattern of the pristine Te NW can be indexed as the [1-74] zone axis of Te. The potassiated products are the K_2Te_3 and K_5Te_3 phases. It is noteworthy that the depotassiated product is single crystal Te (indexed as along the [-130] zone axis), indicating robust reversibility in cycling. Combined with the results of in situ TEM and in situ XRD, the conversion reactions of the Te electrode can be summarized as:

$$3Te + 2K^+ + 2e^- \leftrightarrow K_2Te_3 \quad (1)$$

$$K_2Te_3 + 3K^+ + 3e^- \leftrightarrow K_5Te_3 \quad (2)$$

It is noted that the intermediate K_2Te_3 phase incompletely transforms into the K_5Te_3 phase in the alloying reaction.

3. Conclusion

In conclusion, we have carefully investigated the (de)potassiation process of Te NW by combining in situ HRTEM imaging, SAED, and in situ XRD. Te NWs have a two-step phase transformation: Te to K_2Te_3 in the first stage and incompletely K_2Te_3 to K_5Te_3 in the second stage. During depotassiation, K_2Te_3 and K_5Te_3 phases reversibly transform back to the Te phase. In this work, the atomically resolved, dynamic (de)potassiation process in single crystal Te NWs is observed for the first time. A dynamic anisotropic reaction is revealed that K^+ preferentially intercalates into Te crystalline along the (001) plane in potassiation and reversibly extracted from polycrystal K_2Te_3/K_5Te_3 along the same diffusion path in the depotassiation. The anisotropic reaction of Te NWs on (de)potassiation revealed by the work provides insights into designing nanostructured electrodes for PIBs.

4. Experimental Section

Method: All chemicals were purchased from Sigma–Aldrich and used as received without any further purification. Te NWs were synthesized through a hydrothermal method. In a typical synthesis, 1 g poly(vinylpyrrolidone) (PVP, $M_w \approx 4000$) and 0.089 g Na_2TeO_3 were dissolved in 30 mL of distilled water in a beaker, followed by adding 1.65 mL hydrazine hydrate (85 wt%) and 3.5 mL of aqueous ammonia (25–28 wt%). After being magnetically stirred for 20 min, the mixture was transferred into a 50 mL Teflon-lined stainless-steel autoclave and maintained at 180 °C for 3 h. After quickly cooling to room temperature, 100 mL acetone was added, and the mixture was filtrated and washed several times with H_2O to collect single-phase Te NWs and then dried in an oven at 70 °C.

Nanobattery Setup: The morphology and microstructure evolutions were studied by in situ TEM and in situ ED, respectively. TEM images and ED patterns were acquired at an aberration-corrected Thermo Fisher electron microscope (Titan Cubed Themis G2) operated at 300 kV. The Cs value was ≈6.8 µm. HRTEM images were acquired at a magnification of ◊145 000. The correction of drift was achieved using the Gatan DigitalMicrograph software by the cross-correlation method. In situ TEM was performed by a TEM–STM in situ sample holder (ZepTools Co. Ltd., China) on the Titan Themis STEM. Te NWs were mounted on half copper mesh and used as a cathode. Potassium metals were picked up by a tungsten probe and acted as the counter electrode in the PIBs. The naturally oxidized K_2O layer during transferring the sample holder into TEM acted as the solid electrolyte. The counter electrode was accurately controlled to touch the Te working electrode, then potassiation and depotassiation experiments could be conducted by applying –1 V potential.

Characterization: The crystallographic characteristics of the final products were measured using a Bruker D8 Discover X-ray diffractometer equipped with a Cu Kα radiation source. In situ XRD was employed to analyze the crystal structure evolution and phase transition mechanism during the charging/discharging process. Galvanostatic charge–discharge measurements were performed using a multichannel battery testing system (LAND CT2001A). The XRD signals were acquired every 120 s using a Bruker D8 Discover X-ray diffractometer with a planar detector in still mode. SEM images were collected using a JEOL-7100F scanning electron microscope.

Supporting Information

Supporting Information is available from the Wiley Online Library or from the author.

Acknowledgements

This work was supported by the National Natural Science Foundation of China (52072282). The S/TEM work was performed at the Nanostructure Research Center (NRC), which is supported by the Fundamental Research Funds for the Central Universities (WUT: 2021III016GX). The Key Research and Development Program of Hubei Province (2021BAA070).

Conflict of Interest

The authors declare no conflict of interest.

Author contributions

F.L. and J.M. contributed equally to this work. J.W., F.L., and J.M. conceived the project. F.L. and J.M. synthesized the materials and conducted the electrochemical tests. F.L., R.Y., H.W., S.C., and P.G. performed electron microscopy imaging, spectroscopy experiments, and analysis. F.L. and J.M. prepared the manuscript with contributions and feedback from all authors.

Data Availability Statement

The data that support the findings of this study are available from the corresponding author upon reasonable request.

Keywords

anisotropic reaction mechanisms, atomic scale images, in-situ transmission electron microscopy, K-Te batteries

Received: February 8, 2022
Revised: April 27, 2022
Published online: June 24, 2022

[1] R. Rajagopalan, Y. Tang, X. Ji, C. Jia, H. Wang, *Adv. Funct. Mater.* **2020**, *30*, 1909486.
[2] J. C. Pramudita, D. Sehrawat, D. Goonetilleke, N. Sharma, *Adv. Energy Mater.* **2017**, *7*, 1602911.
[3] B. Wang, Y. Peng, F. Yuan, Q. Liu, L. Sun, P. Zhang, Q. Wang, Z. Li, Y. A. Wu, *J. Power Sources* **2021**, *484*, 229244.
[4] F. Liu, J. Meng, G. Jiang, J. Li, H. Wang, Z. Xiao, R. Yu, L. Mai, J. Wu, *Matter* **2021**, *4*, 4006.
[5] K. T. Chen, H. Y. Tuan, *ACS Nano* **2020**, *14*, 11648.
[6] J. Huang, X. Lin, H. Tan, B. Zhang, *Adv. Energy Mater.* **2018**, *8*, 1703496.
[7] Y. Wang, P. Niu, J. Li, S. Wang, L. Li, *Energy Storage Mater.* **2021**, *34*, 436.
[8] X. L. Huang, Z. Guo, S. X. Dou, Z. M. Wang, *Adv. Funct. Mater.* **2021**, *31*, 2102326.
[9] R. Xu, Y. Yao, H. Wang, Y. Yuan, J. Wang, H. Yang, Y. Jiang, P. Shi, X. Wu, Z. Peng, Z. S. Wu, J. Lu, Y. Yu, *Adv. Mater.* **2020**, *32*, 2003879.
[10] Y. Yao, R. Xu, M. Chen, X. Cheng, S. Zeng, D. Li, X. Zhou, X. Wu, Y. Yu, *ACS Nano* **2019**, *13*, 4695.
[11] Q. Li, H. Liu, Z. Yao, J. Cheng, T. Li, Y. Li, C. Wolverton, J. Wu, V. P. Dravid, *ACS Nano* **2016**, *10*, 8788.
[12] Y. Li, J. Lu, X. Cheng, H. Shi, Y. Zhang, *Nano Energy* **2018**, *48*, 441.

[13] J. He, Y. Chen, W. Lv, K. Wen, Z. Wang, W. Zhang, Y. Li, W. Qin, W. He, *ACS Nano* **2016**, *10*, 8837.
[14] J. Ding, H. Zhang, W. Fan, C. Zhong, W. Hu, D. Mitlin, *Adv. Mater.* **2020**, *32*, 1908007.
[15] J. K. Kim, Y. C. Kang, *ACS Nano* **2020**, *14*, 13203.
[16] S. Dong, D. Yu, J. Yang, L. Jiang, J. Wang, L. Cheng, Y. Zhou, H. Yue, H. Wang, L. Guo, *Adv. Mater.* **2020**, *32*, 1908027.
[17] Q. Liu, W. Deng, C.-F. Sun, *Energy Storage Mater.* **2020**, *28*, 10.
[18] J. He, W. Lv, Y. Chen, K. Wen, C. Xu, W. Zhang, Y. Li, W. Qin, W. He, *ACS Nano* **2017**, *11*, 8144.
[19] J. Cui, H. Zheng, Z. Zhang, S. Hwang, X.-Q. Yang, K. He, *Matter* **2021**, *4*, 1335.
[20] J. Chen, Y. Cheng, Q. Zhang, C. Luo, H. Y. Li, Y. Wu, H. Zhang, X. Wang, H. Liu, X. He, J. Han, D. L. Peng, M. Liu, M. S. Wang, *Adv. Funct. Mater.* **2020**, *31*, 2007158.
[21] M. Yousaf, U. Naseer, Y. Li, Z. Ali, N. Mahmood, L. Wang, P. Gao, S. Guo, *Energy Environ. Sci.* **2021**, *14*, 2670.
[22] X. Ge, L. Yin, *Energy Storage Mater.* **2019**, *20*, 89.
[23] J. Xie, J. Li, W. Mai, G. Hong, *Nano Energy* **2021**, *83*, 105780.
[24] X. Wu, S. Li, B. Yang, C. Wang, *Electrochem. Energy Rev.* **2019**, *2*, 467.
[25] Q. Li, Z. Yao, E. Lee, Y. Xu, M. M. Thackeray, C. Wolverton, V. P. Dravid, J. Wu, *Nat. Commun.* **2019**, *10*, 1692.
[26] Y. Yuan, K. Amine, J. Lu, R. Shahbazian-Yassar, *Nat. Commun.* **2017**, *8*, 15806.
[27] I. Capone, J. Aspinall, E. Darnbrough, Y. Zhao, T.-U. Wi, H.-W. Lee, M. Pasta, *Matter* **2020**, *3*, 2012.
[28] C. Ma, Y. Cheng, K. Yin, J. Luo, A. Sharafi, J. Sakamoto, J. Li, K. L. More, N. J. Dudney, M. Chi, *Nano Lett.* **2016**, *16*, 7030.
[29] Y. Liu, F. Fan, J. Wang, Y. Liu, H. Chen, K. L. Jungjohann, Y. Xu, Y. Zhu, D. Bigio, T. Zhu, C. Wang, *Nano Lett.* **2014**, *14*, 3445.
[30] H. Wang, F. Liu, R. Yu, J. Wu, *Interdiscip. Mater.* **2022**, *1*, 196.
[31] S. Yao, J. Cui, Z. Lu, Z.-L. Xu, L. Qin, J. Huang, Z. Sadighi, F. Ciucci, J.-K. Kim, *Adv. Energy Mater.* **2017**, *7*, 1602149.
[32] K. Wang, Y. Yang, H.-W. Liang, J.-W. Liu, S.-H. Yu, *Mater. Horiz.* **2014**, *1*, 338.
[33] R. Cai, S. Guo, Y. Wu, S. Zhang, Y. Sun, S. Chen, P. Gao, C. Zhu, J. Chen, Z. Zhu, L. Sun, F. Xu, *Energy Storage Mater.* **2021**, *37*, 345.
[34] Y. Wu, W. Luo, P. Gao, C. Zhu, X. Hu, K. Qu, J. Chen, Y. Wang, L. Sun, L. Mai, F. Xu, *Nano Energy* **2020**, *77*, 105299.
[35] X. H. Liu, J. W. Wang, S. Huang, F. Fan, X. Huang, Y. Liu, S. Krylyuk, J. Yoo, S. A. Dayeh, A. V. Davydov, S. X. Mao, S. T. Picraux, S. Zhang, J. Li, T. Zhu, J. Y. Huang, *Nat. Nanotechnol.* **2012**, *7*, 749.
[36] J. Meng, Q. He, L. Xu, X. Zhang, F. Liu, X. Wang, Q. Li, X. Xu, G. Zhang, C. Niu, Z. Xiao, Z. Liu, Z. Zhu, Y. Zhao, L. Mai, *Adv. Energy Mater.* **2019**, *9*, 1802695.
[37] Z. Xiao, J. Meng, F. Xia, J. Wu, F. Liu, X. Zhang, L. Xu, X. Lin, L. Mai, *Energy Environ. Sci.* **2020**, *13*, 3129.
[38] Y. Wu, X. Xu, C. Zhu, P. Liu, S. Yang, H. L. Xin, R. Cai, L. Yao, M. Nie, S. Lei, P. Gao, L. Sun, L. Mai, F. Xu, *ACS Energy Lett.* **2019**, *4*, 2081.